Nanoscale

Accepted Manuscript

This article can be cited before page numbers have been issued, to do this please use: W. Guo, X. Wang, X. Pu, W. Xiang, C. Yang, Y. Zhang and Z. Fang, *Nanoscale*, 2025, DOI: 10.1039/D5NR02407B.

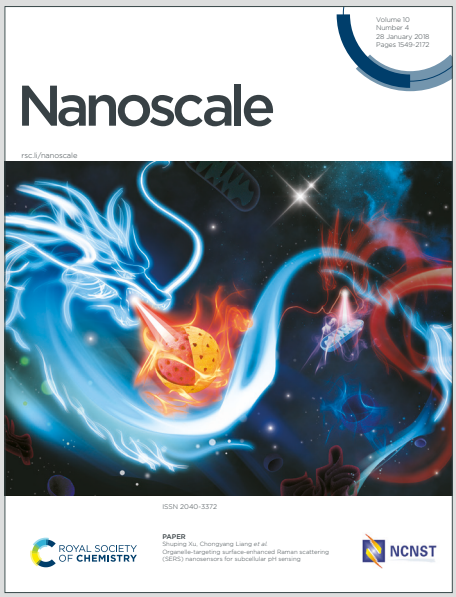

ROYAL SOCIETY OF CHEMISTRY

rsc.li/nanoscale

ROYAL SOCIETY OF CHEMISTRY
View Article Online
DOI: 10.1039/D5NR02407B

Nanoscale

PAPER

Metal/TiO_2 composite photocatalysts with tunable activity for nitrogen fixation: The impact of metal nanoparticles†

Cite this: *Nanoscale*, 20xx, x, xxx

Wenjie Guo,[‡a] Xuejing Wang,[‡a] Xiao-Li Pu,[‡b] Wenlong Xiang,[a] Chao Yang,[b] Yanhui Zhang*[a] and Zhi-Bin Fang*[b]

Received 00th January 20xx,
Accepted 00th January 20xx

DOI: 10.1039/x0xx00000x

rsc.li/nanoscale

Photocatalytic N_2 fixation reactions can harvest solar energy to convert the abundant but inert N_2 into available NH_4^+. Nanoscale metal/semiconductor composites are among the most developed photocatalysts for the conversion, whereas systematic investigations for the impact of metal species and status on their photocatalytic performance are rarely reported. Herein, metal nanoparticle-modified TiO_2 (M-TiO_2, M =Au, Pd, Cu) were selected as model composites for photocatalytic N_2 fixation. By varying the metal species and reductants in the synthesis, the obtained M-TiO_2 exhibited tunable photocatalytic activities for nitrogen fixation. Among them, Cu-TiO_2 prepared with sodium borohydride performed the highest rate of NH_4^+ production (16.3 $mg \cdot L^{-1} \cdot h^{-1}$). Mechanism studies revealed that the high activity of Cu-TiO_2 was attributed to the synergistic effect among the small size of Cu NPs (2-6 nm), the enhanced interfacial interactions, and the high usage of photogenerated electrons. This work may guide the design of efficient metal/semiconductor photocatalysts for nitrogen fixation and other energy conversion reactions.

Introduction

Ammonia is of extraordinary significance to the development of living organisms and a sustainable society. In nature, ammonia (NH_3) is an important raw material for fertilizer production and plays a critical role in agriculture, industrial development, and energy conversion/storage. Fixing nitrogen and converting it to ammonia is an effective way to realize the nitrogen cycle in the ecosystem. Notably, the conversion of nitrogen to ammonia requires the breaking of the N≡N bond in nitrogen.[1-3] Because of the robust N≡N bond, which has an extremely high bond energy (940 $kJ \cdot mol^{-1}$) of nitrogen, breaking the N≡N bond is challenging.[4-6] Thus, artificial nitrogen fixation is highly desired. Undeniably, the industrial Haber-Bosch strategy is the most effective artificial ammonia synthesis technology. However, this process consumes a lot of energy and releases significant amounts of greenhouse gases. It is essential to develop green and cost-effective technologies for ammonia synthesis. Much effort has been devoted to developing artificial nitrogen fixation methods, including photocatalysis and electrocatalysis.[7-11] Among them, photocatalytic nitrogen fixation uses green and pollution-free renewable solar energy as the primary energy source, nitrogen as the raw material, and water as a reducing agent to produce ammonia, which is considered the most promising method.[12-16]

Various materials are used as photocatalysts to synthesize ammonia, including BiOX, Bi_2MoO_6, $BiVO_4$, TiO_2, CdS, In_2S_3, g-C_3N_4, hydrogen-bonded organic frameworks and so on.[17-20] TiO_2 has been widely reported as a high-quality photocatalyst in industrial, pharmaceutical, agricultural applications due to its excellent stability, non-toxicity, and low cost.[21-23] P25 is a commercial TiO_2 with both anatase and rutile crystal phases (80:20). The increased photocatalytic activity of P25 compared with monocrystal TiO_2 is attributed to the fact that rutile acts as an electronic receiver, facilitating the separation of photogenerated carriers in anatase. At the same time, acting as the active component allows the holes in anatase to migrate to the TiO_2 surface.[24] However, due to the low charge separation efficiency of P25, the improvement of photocatalytic performance is not significant. Therefore, modifications are needed to facilitate vector separation and increase activity.[25-27] Previous studies confirm effective strategies for improving the photocatalytic activity of TiO_2 (P25), including doping, defects, loading, and surface modification.[28-31] Surface modification is one of the most effective strategies for improving the photocatalytic performance of catalysts. The surface modification can improve the light absorption capacity of the supported materials in the visible region of the solar spectrum, and thus improve the photochemical properties of the supported

[a]*College of Chemistry, Chemical Engineering and Environment, Fujian Province Key Laboratory of Morden Analytical Science and Separation Technology, Minnan Normal University, Zhangzhou, 363000, P.R. China*
E-mail: zhangyh@mnnu.edu.cn;
[b]*State Key Laboratory of Structural Chemistry, Fujian Institute of Research on the Structure of Matter, Chinese Academy of Sciences, Fuzhou, 350002, P.R. China.*
E-mail: fangzhibin@fjirsm.ac.cn
†Supplementary Information (SI) available: Fig. S1-S10, Tables S1 and S2,.See DOI: 10.1039/x0xx00000x
‡These authors contributed equally to this work.

View Article Online
DOI: 10.1039/D5NR02407B

materials.[32-33] At the same time, it can promote the migration of photogenerated carriers, thus reducing the recombination of electron-hole pairs.[34-37]

In recent years, various elements have been investigated for TiO_2 loading/modification. The precious metals Au and Pd are considered the most promising co-catalysts for improving photocatalytic performance. Because they can alter the charge transfer characteristics between TiO_2 and the surrounding environment when modifying TiO_2, thereby enhancing the photocatalytic activity of TiO_2 materials.[38-40] In addition, non-noble metals (Fe, Cu, Zn, etc.) can extend the light absorption range of TiO_2 to the visible light region.[41-44] Among these transition metals, Cu is an excellent modifier to adjust the low efficiency of TiO_2 in charge separation. Because it allows light absorption to extend into the visible region, it can also act as a charge-carrier catcher, thus inhibiting photogenerated electron-hole pair recombination.[45-47] However, there are few systematic reports focusing on the impact of species and status of metal nanoparticles on photocatalytic nitrogen fixation activities of metal-loaded TiO_2 composites.

In this work, different metal-loaded TiO_2 (M-TiO_2, M=Au, Pd, Cu) composites were synthesized via a simple chemical reduction method using ascorbic acid or $NaBH_4$ as reductants. The impact of metal types and particle sizes on the nitrogen fixation performance of M-TiO_2 was discussed. The analysis results showed that the photocatalytic performances of M-TiO_2 could be tuned by the selection of reductants and metal precursors. Cu-TiO_2 prepared with $NaBH_4$ as a reductant exhibited the highest activity for photocatalytic nitrogen fixation with an NH_4^+ production rate of 16.3 $mg \cdot L^{-1} \cdot h^{-1}$. The mechanism for the superior photocatalysis by Cu-TiO_2 was further proposed, which originated from the synergistic effect among the small size of Cu NPs (2-6 nm), the enhanced interfacial interactions, and the high usage of photogenerated electrons.

Experimental section

Preparation

Reagents. Palladium chloride ($PdCl_2$), sodium metaborate ($NaBH_4$), and gold trichloride ($AuCl_3 \cdot HCl \cdot 4H_2O$) were obtained from Sinopharm Chemical Reagent Co., Ltd. Titanium dioxide (P25) was obtained from Evonik Industries AG (Shanghai). Ascorbic acid and copper chloride dihydrate ($CuCl_2 \cdot 2H_2O$) were obtained from Xilong Chemical Co., Ltd. Ethanol, ethylene glycol and seignette salt were obtained from Xilong Science Co., Ltd. Nessler's reagent was obtained from Changde Beekman Biotechnology Co., Ltd. All the chemical reagents without any further purification processes, were of analytical grade and used directly.

Synthesis. M-TiO_2 (M=Au, Pd, Cu) catalysts were synthesized via a simple chemical reduction method using ascorbic acid or $NaBH_4$ as reductants (Scheme 1). The loadings of metal NPs were 2 wt%, which is a reasonable loading based on our previous reports.[48,49] $HAuCl_4$, H_2PdCl_4, and $CuCl_2$ were selected as the metal precursors.

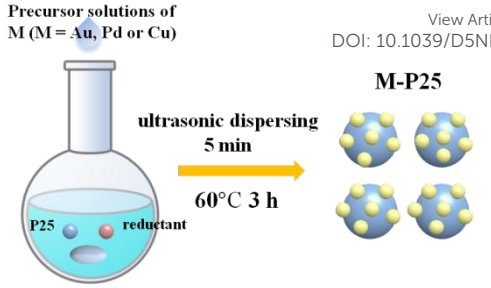

Scheme 1 Schematic diagram for the synthesis of M-P25.

Typically, 0.2 g of TiO_2 nanoparticles and 4.5 mmol of reductant were dispersed in 150 mL of deionized water after ultrasonic treatment for 5 min to form a uniform mixture. The desired volume of as-prepared metal precursor solutions was added dropwise to the mixture, followed by stirring in an oil bath at 60°C for 3 h. Finally, the solid products were obtained, washed with ethanol and water three times, and dried in a vacuum oven at 60℃ for 12 h. The catalysts synthesized with $NaBH_4$ and ascorbic acid as reductants were named M-TiO_2-S1 and M-TiO_2-S2, respectively.

Characterization

The crystalline structures of the as-prepared samples were characterized by powder X-ray diffraction (XRD) analysis using an Ultima IV X-ray diffractometer (Rigaku, Japan) with Cu-Kα1 radiation (λ=0.15406 nm) operated at 40 kV and 40 mA in the range from 5° to 80°. The transmission electron microscopic (TEM) images and high-resolution TEM (HRTEM) images were taken on a Tecnai G2 F20 microscope (FEI, US) with a high-angle annular dark-field detector to observe the morphology of the samples. The elemental composition of the obtained samples and the chemical states were investigated by X-ray photoelectron spectroscopy (XPS, Thermo ESCALAB 250XI) and the Fourier-transform infrared spectroscopy (FT-IR, Nicolet iS 10) with a resolution of 4 cm^{-1}. The UV-Vis diffuse reflectance spectroscopy (DRS) was conducted using a UH4150 model ultraviolet-visible near-infrared spectrophotometer. The light absorption range and capacity of samples were determined by UV-Vis DRS with $BaSO_4$ as the internal reflectance standard over a wavelength range of 200-800 nm. The Brunauer-Emmett-Teller (BET) specific surface areas and pore structures of the as-prepared samples were analyzed using a N_2 adsorption-desorption isotherm apparatus (Quadrasorb evoTM, US). Ion chromatography (ICS-1100, US) was used to determine the ammonia yield. The contents of metals were quantitatively analyzed on an Inductively Coupled Plasma Optical Emission Spectrometry (ICP-OES, Agilent 720ES).

Test of photocatalytic activity

The photocatalytic performance of N_2 fixation for the as-prepared catalysts was estimated based on the production rate of NH_4^+ in a double-walled quartz reactor. A 300 W Xenon lamp (PLS-SXE300C, Beijing Perfectlight Co. Ltd) was used as a light source in the nitrogen fixation reactions. In a typical photocatalytic experiment, 25 mg of the photocatalyst was dispersed in a 130 mL mixture of ethylene glycol and deionized water (volume ratio 1:9). Before turning on the light, the mixed

solution was stirred in the dark while high-purity N_2 bubbled on for 30 min to remove air interference and achieve the adsorption-desorption equilibrium in the system. During the photocatalysis process, an external cooling water circulation system was used to maintain the reaction temperature at 20 °C. The distance from the light source to the liquid surface was 11 cm. 5 mL of the liquid sample was taken out at 1 h intervals and filtered through the 0.22 μm membrane filter. The reaction lasted for 6 h, and the content of the product in the reactor was measured every 1 h. The NH_4^+ concentration was determined using Nessler's reagent method and was detected by UV-Visible spectrophotometry at 420 nm of the absorption wavelength.[26,50]

Photoelectrochemical measurements

The electrochemical impedance spectroscopy (EIS) and transient photocurrent response were measured on a CHI660D electrochemical workstation (Chenhua, China). The working electrode was prepared using fluorine-doped tin oxide (FTO, 1×2 cm) glass previously cleaned via ultrasonication in ethanol for 30 min, followed by drying at 60 °C. A total of 10 mg of sample was dispersed in 1 mL of deionized water and deposited onto the pretreated FTO glass surface. In addition, Ag/AgCl and a Pt network were used as the reference and the counter electrodes, respectively. The electrolyte solution used in the electrochemical test was a 0.5 M Na_2SO_4 solution.

Results and discussion

The crystalline features and chemical structures of as-prepared samples were determined via X-ray diffraction (XRD) patterns and Fourier transform infrared (FTIR) spectroscopy. As shown in Fig. 1, characteristic diffraction peaks at approximately 25.3°, 27.6°, 37.8°, 48.0°, 53.9°, 55.1° and 62.6° correspond to the crystallographic planes of (101), (110), (004), (200), (105), (211), and (204), respectively. All the diffraction patterns of TiO_2 (P25) and M-TiO_2 were consistent with those of anatase (JCPDS, No. 21-1272) and rutile TiO_2 (JCPDS, No. 21-1276). However, the diffraction peaks of Au, Pd, and Cu NPs were not observed in any of the M-TiO_2 samples, which may be attributed to the small particle sizes and low doping contents of metal NPs (Fig. S1†). As shown in the FT-IR spectrum of the TiO_2 and M-TiO_2 samples (Fig. S2†), the broad bands at approximately 3433 cm^{-1} and 1638 cm^{-1} were attributed to the bending vibration of O-H and the symmetric stretching vibration of Ti-O, respectively, which agrees well with TiO_2. These results suggest that the chemical structure of TiO_2 was maintained upon loading metal NPs. To investigate the surface element composition and the elemental states of M-TiO_2, all samples were analyzed by X-ray photoelectron spectroscopy (XPS). As can be seen from Fig. S3a,† the XPS survey spectra of Cu-TiO_2 catalyst confirmed the existence of C, Ti, and O elements. However, it was found that the Cu 2p signal was not detected on Cu-TiO_2-S2 sample. This result suggests that the reductant ascorbic acid hardly reduced Cu^{2+} to Cu NPs. In contrast, the XPS survey spectra of all Au-TiO_2 and Pd-TiO_2 catalysts exhibited the presence of C, Ti, O, and either Au or Pd elements, indicating that both ascorbic acid and $NaBH_4$ reductants can successfully reduce precious metals Au and Pd (Fig. S3b and S3c†). In addition, the high-resolution Cu 2p spectrum is depicted in Fig. 2a, exhibiting two higher peaks ascribed to Cu^0 $2p_{1/2}$ and $2p_{3/2}$, and the other two assigned to Cu^{2+} $2p_{1/2}$ and Cu $2p_{3/2}$, respectively. As shown in Fig. 2b, the high-resolution spectrum of Au displays peaks at approximately 87.3 eV and 83.5 eV, corresponding to two distinct spin-orbit pairs, Au^0 $4f_{5/2}$ and Au $4f_{7/2}$. In addition, the high-resolution spectrum of Pd displays peaks at approximately 340.6 eV and 335.3 eV, corresponding to two distinct spin-orbit pairs, Pd^0 $3d_{5/2}$ and Pd $3d_{3/2}$ (Fig. 2c and 2d). The other two peaks observed at approximately 336.5 eV and 341.5 eV belong to Pd^{2+}, indicating a low loading amount of Pd^{2+} in Pd-TiO_2-S2. These analysis results suggest that the M-TiO_2 samples have been successfully prepared, except for Cu-TiO_2-S2.

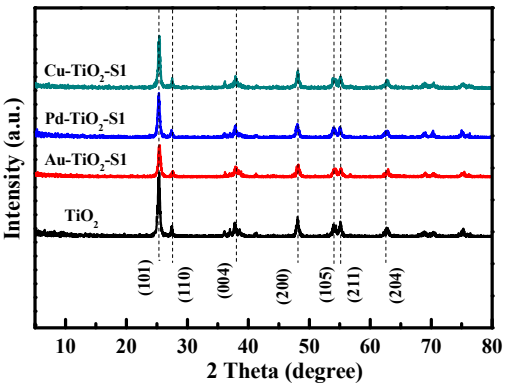

Fig. 1 XRD patterns of TiO_2 and M-TiO_2-S1.

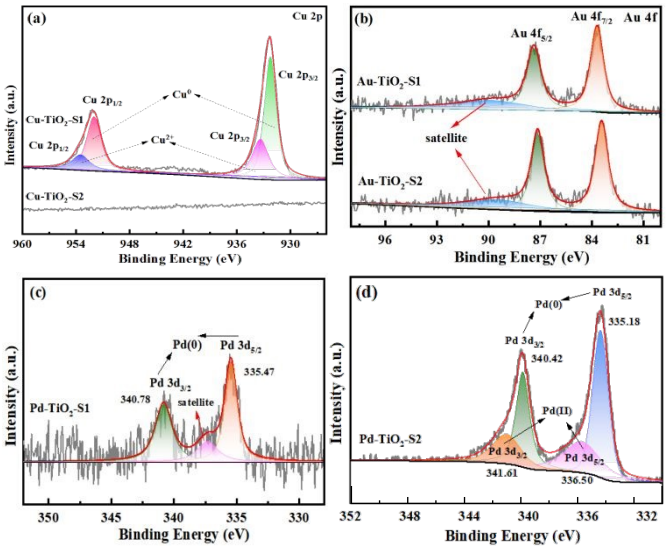

Fig. 2 The high-resolution XPS survey spectra of Cu-TiO_2 (a), Au-TiO_2 (b) and Pd-TiO_2 (c, d).

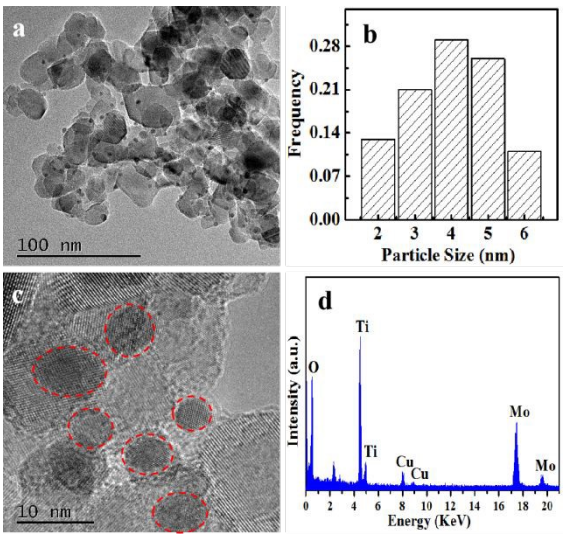

Fig. 3 TEM images (a, c), size distribution of Cu NPs (b), and energy-dispersive X-ray spectra (d) of Cu-TiO_2-S1.

To further demonstrate the formation of Au, Pd, and Cu NPs on the TiO_2 surface, we performed transmission electron microscopy (TEM) analysis of M-TiO_2-S1 (M = Au, Pd, and Cu). As shown in Fig. 3, Fig. 4, and Fig. S4,† Au, Pd, and Cu NPs were all uniformly dispersed on the surface of TiO_2. The size distribution analysis shows that the size of Cu NPs is in the range of 2-6 nm (Fig. 3b). In addition, the EDS (Energy Dispersive Spectroscopy) spectrum demonstrates that Cu-TiO_2-S1 contains Ti, O and Cu elements (Fig. 3d). The Mo elements mainly come from the molybdenum mesh support for TEM testing. Furthermore, when $NaBH_4$ was used as a reductant, Au NPs had a particle size distribution of about 2-6 nm, which is smaller than that of Pd NPs (3-8 nm), as shown in Fig. 4. However, when we replaced the reductant with ascorbic acid, the size of Au NPs increased significantly (5-20 nm), while the size of Pd NPs did not change (Fig. S4b and S4d†). This obvious difference in particle size changes explains

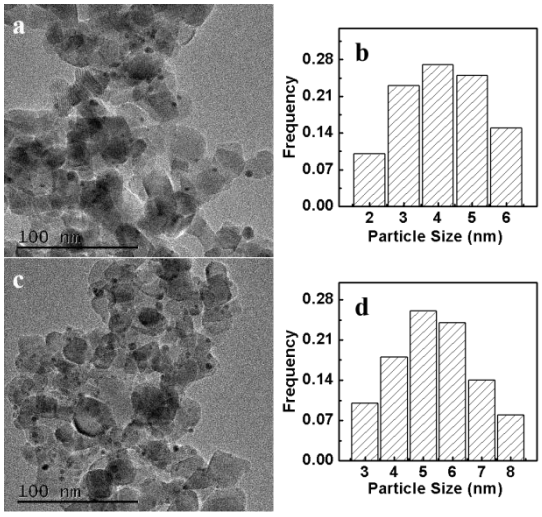

Fig. 4 TEM images and size distribution of Au-TiO_2-S1 (a, b) and Pd-TiO_2-S1 (c, d)

the main reason why the selection of the two reductants has little effect on the catalytic performance of Pd-TiO_2, but a significant effect on Au-TiO_2, which we refer to as the size effect. In conclusion, both Au and Cu NPs reduced by $NaBH_4$ have the advantage of a smaller size.

The performance of the photocatalytic nitrogen fixation of all samples was evaluated, as shown in Fig. 5a and 5b. The total amount of ammonia nitrogen was measured by Nessler's reagent spectrophotometry, and the standard curve is shown in Fig. S5.† Compared with the previous preparation methods of TiO_2 loaded metals for photocatalytic reactions, the preparation method described in this paper is simpler.[40-42] Furthermore, previous studies have not systematically compared the effects of different reductants on the nitrogen fixation activity of noble metal and transition metal loaded TiO_2. In addition, the nitrogen-fixing performance of different types of catalysts was compared, as shown in Table S1†. From Fig. 5a, it can be seen that the nitrogen fixation activity of M-TiO_2-S1 composites has improved to a certain extent compared with pure TiO_2. The as-prepared Cu-TiO_2-S1 exhibited the best photocatalytic nitrogen fixation performance under simulated sunlight, achieving a rate of up to 16.3 $mg \cdot L^{-1} \cdot h^{-1}$, indicating that its utilization of photogenerated carriers is very efficient (Fig. 5c). For both $NaBH_4$ and ascorbic acid, the yield of Pd-TiO_2 shows that the choice of reductant has little effect on the performance of photocatalytic nitrogen fixation in Pd-TiO_2. Ordinarily, a smaller particle radius provides more reactive sites, which leads to a better catalytic effect. In the case of Au-TiO_2, the Au NPs reduced by $NaBH_4$ have a smaller size (2-6 nm), resulting in an ammonia yield when $NaBH_4$ is used as a reductant that is three times higher than that obtained with ascorbic acid. Thus, the choice of reductant greatly influences the performance of photocatalytic nitrogen fixation in Au-TiO_2.

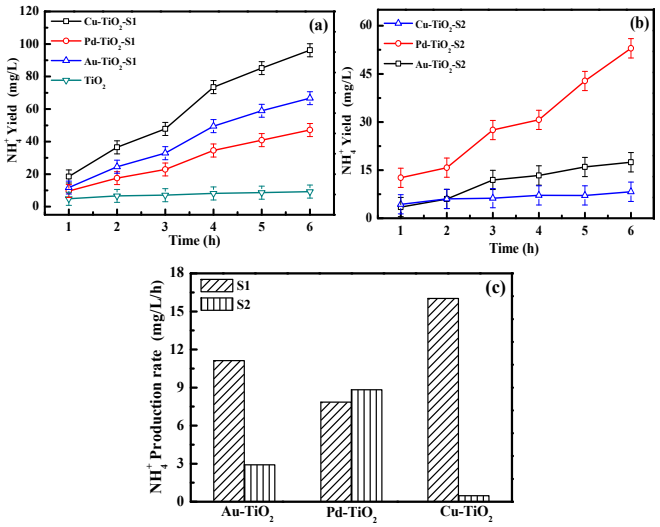

Fig. 5 The ammonia yield of TiO_2, M-TiO2-S1 (a) and M-TiO_2-S2 (b); the average ammonia production rate of M-TiO_2 (c).

Last but not least, we found that the choice of reductant had the most significant impact on the photocatalytic N_2 fixation

ability of Cu-TiO_2. The ammonia production rate of Cu-TiO_2-S1 is the highest, 33.5 times greater than that of Cu-TiO_2-S2, primarily due to the weak reducing ability of ascorbic acid, which cannot reduce Cu.

Following the blank experiments and control experiments tests for photocatalytic nitrogen fixation, the results of the blank experiments showed that hardly any nitrogen fixation activity was observed in the absence of a catalyst, N_2, or light irradiation. In addition, we used argon instead of N_2 in the reaction. It was found that almost no ammonia was detected under an argon atmosphere in the presence of Cu-TiO_2-S1, indicating that N_2 was the primary source of ammonia synthesis, as shown in Fig. S6a.† To verify the reliability of the ammonia yield determined by the Nessler's reagent method, ion chromatography was used to further assess the ammonia yield. A characteristic peak of NH_4^+ was observed in the ion chromatogram (Fig. S6b†). The analysis results show that the ammonia yield detected by ion chromatography was consistent with that obtained by the Nessler's reagent method. In addition, XRD patterns after the reaction showed the same diffraction peaks as before, and no diffraction peaks of CuO and Cu_2O were found (Fig. S6c†), indicating that Cu-TiO_2-S1 has good stability.

The above results show a significant difference in the photocatalytic activity of different M-TiO_2 composites prepared with ascorbic acid and $NaBH_4$ as reductants. To explore the main reasons for the differences in the nitrogen fixation performance, we further conducted optical properties and photoelectrochemical characterization of the catalysts. We used the UV-Vis diffuse reflection spectrum (DRS) to investigate the optical absorption properties of the prepared samples. As shown in Fig. 6, the characteristic absorption edges of M-TiO_2-S1 were located in the visible region. Au-TiO_2-S1 exhibits the strongest light absorption. However, Au-TiO_2-S1 displayed the lowest activity for nitrogen fixation among the M-TiO_2-S1 catalysts (Fig. 5). Although Cu-TiO_2-S2 exhibited higher light absorption than Cu-TiO_2-S1 (Fig. S7a†), there was a 12-fold increase in the nitrogen fixation activity of Cu-TiO_2-S1 compared to Cu-TiO_2-S2. Similarly, the DRS of Au-TiO_2 indicated that Au-TiO_2-S2 had better light absorption ability than Au-TiO_2-S1 (Fig. S7b†). Notably, a strong peak at about 550 nm appeared in the visible region, attributed to the localized surface plasmon resonance effect of Au NPs. Nevertheless, the nitrogen fixation activity of Au-TiO_2-S2 is much lower than that of Au-TiO_2-S1. For Pd-TiO_2, although there is a significant difference in their light absorption characteristics (Fig. S7c†), Pd-TiO_2-S1 and Pd-TiO_2-S2 demonstrate almost the same nitrogen fixing performance. From the analysis results of the optical properties, it was found that the optical absorption characteristics of M-TiO_2 are independent of their nitrogen fixation activity. Thus, it can be speculated that the differences in photocatalytic nitrogen fixation activity of M-TiO_2 may not be due to their optical absorption properties.

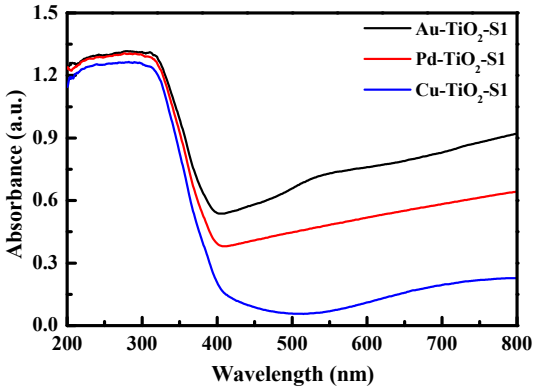

Fig. 6 The UV-Vis optical absorption curves of M-TiO_2-S1.

To acquire more structural information about the samples, the specific surface areas and average pore sizes of M-TiO_2-S1 were investigated using nitrogen adsorption-desorption isotherms. M-TiO_2-S1 exhibits a type IV (H3 hysteresis loops) absorption isotherm, which corresponds to the characteristics of mesoporous materials (Table S2 and Fig. S8†). Generally, large specific surface areas are beneficial for exposing more active sites, thereby promoting photocatalytic performance. In addition, mesoporous materials allow reactants to react more efficiently. The specific surface areas of Au-TiO_2-S1, Pd-TiO_2-S1 and Cu-TiO_2-S1 were 48, 45, and 46 $m^2 \cdot g^{-1}$, respectively (Table S2†). It can be noted that there is no significant difference in the specific surface area, suggesting that the specific surface area is not the major influencing factor for photocatalytic nitrogen fixation performance.

Photoelectrochemical measurements, including the transient photocurrent and EIS spectra, were used to confirm the ability of the as-prepared catalysts to separate intrinsic charges. It is widely acknowledged that the smaller charge transfer resistance, the more favorable the transfer of photogenerated carriers in the photocatalytic system. As shown in Fig. 7a, among the samples of M-TiO_2-S1, the Nyquist curve radius of Cu-TiO_2-S1 is the smallest, indicating that the electrochemical reaction kinetics are the fastest. This suggests that Cu-TiO_2-S1 has the highest ability to transfer photogenerated carriers, which is consistent with the activity observed in photocatalytic nitrogen fixation. It is noted that the charge transfer resistance of Cu-TiO_2-S1 and Au-TiO_2-S1 is significantly lower than that of Cu-TiO_2-S2 and Au-TiO_2-S2, respectively. This indicates that $NaBH_4$ is more suitable than ascorbic acid as a reductant for preparing M-TiO_2 catalysts using Cu and Au precursors (Fig. S9a and S9b†). Furthermore, the samples exhibit a sensitive response under visible-light irradiation, with the order of photocurrent values being Cu-TiO_2-S1 > Au-TiO_2-S1 > Pd-TiO_2-S1 (Fig. 7b), which aligns with the photocatalytic performance shown in Fig. 5. The photocurrent analysis results reveal that Cu-TiO_2-S1 is more favorable to promoting electron-hole separation and improving the utilization of photo-electrons. In contrast to Cu-TiO_2-S1 and Au-TiO_2-S1 reduced by $NaBH_4$, a significant difference in photocurrent intensity was observed for Cu-TiO_2-S2 and Au-TiO_2-S2 reduced by ascorbic acid (Fig. S9c and S9d†). Cu-TiO_2-S1 and Au-TiO_2-S1 reduced by $NaBH_4$ indeed show stronger photocurrent intensity. The result

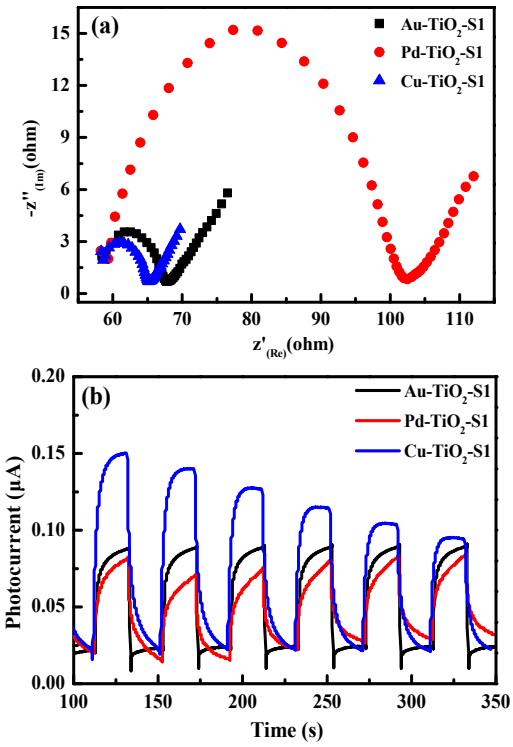

Fig. 7 EIS spectra of M-TiO_2-S1 (a); transient photocurrent response measurements under visible-light irradiation of M-TiO_2-S1 (b).

shows that it has better photon-generated carrier separation and migration ability. The analyses confirm that Cu-TiO_2-S1 exhibits good interfacial charge transfer ability, thereby promoting photoexcited electron-hole separation, which is crucial for enhancing the photocatalytic nitrogen fixation performance of Cu-TiO_2. This may also explain the differences in nitrogen fixing performance of M-TiO_2 synthesized by different reductants.

Based on the analysis results above, we propose a feasible photocatalytic N_2 fixation mechanism for the Cu-TiO_2-S1 catalyst. Through the valence band spectrum and band gap diagram, we calculated the conduction and valence band positions of TiO_2 to be -0.28 eV and 2.9 eV, respectively (Fig. S10a and S10b†). As shown in Fig. 8, the photogenerated electrons (e^-) and holes (h^+) are generated on the surface of the TiO_2 (P25) nanoparticles under simulated-solar-light irradiation. When irradiated, photo-induced electrons on TiO_2 transfer to the transition metal Cu^0/Cu^{2+} surface for nitrogen fixation reaction, while holes oxidize ethylene glycol. During this process, the binding of the titanium site to the Cu^0/Cu^{2+} surface induces favorable electron migration. As a result of the rapid transfer of electrons to Cu^0/Cu^{2+}, chemically adsorbed N_2 molecules on the metal sites are activated, thus reducing the activation barrier and improving the utilization rate of photogenerated carriers. Therefore, the high photocatalytic activity of Cu-TiO_2-S1 can be attributed to strong electronic interactions. Firstly, the small size of the Cu^0/Cu^{2+} NPs provides more active sites that accept more electrons, thus prolonging the lifetime of

View Article Online
DOI: 10.1039/D5NR02407B

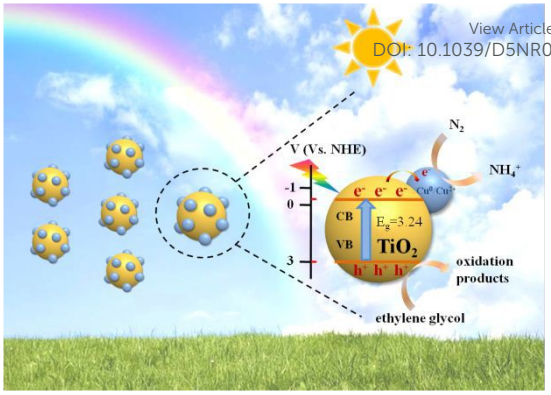

Fig. 8 The feasible mechanism of photocatalytic nitrogen fixation of Cu-TiO_2-S1 under simulated-solar-light irradiation.

charge carriers. Secondly, the enhanced interfacial interaction between Cu and TiO_2 facilitates the conduction of photogenerated electrons, thereby further reducing the recombination of photogenerated electron-hole pairs and enhancing the efficiency of photocatalytic nitrogen fixation in Cu-TiO_2-S1.

Conclusions

In summary, a series of metal-loaded TiO_2 (M-TiO_2, M = Au, Pd, Cu) photocatalysts were synthesized via facile chemical reduction with different reductants. The reductants affected the particle sizes and the reduction degrees of loaded metals. With further tuning in metal species, the photocatalysis of M-TiO_2 was optimized, among which Cu-TiO_2-S1 demonstrated the highest activity for nitrogen-to-ammonia production (16.3 $mg \cdot L^{-1} \cdot h^{-1}$). Characterizations revealed that the small size of the loaded Cu NPs induced more active sites for photocatalysis and that the strong interaction between Cu and TiO_2 promoted electron-hole separation, leading to more efficient adsorption and activation of N_2 molecules. This work not only showcases advanced materials for photocatalytic nitrogen fixation but also demonstates accessible methods for material optimization toward high activities, which contributes to the design and development of more advanced photocatalysts.

Author contributions

Wenjie Guo: investigation, writing - original draft. Xuejing Wang: investigation, writing - original draft. Xiao-Li Pu: validation, data curation. Wenlong Xiang: project administration. Chao Yang: methodology. Yanhui Zhang: resources, conceptualization, writing - review & editing, supervision, funding acquisition. Zhi-Bin Fang: writing - review & editing, supervision, funding acquisition.

Conflicts of interest

There are no conflicts to declare.

View Article Online
DOI: 10.1039/D5NR02407B

Acknowledgements

This work was supported by the the National Natural Science Foundation of China (21703094, 22272178), the Natural Science Foundation of Fujian Province (2019J01743, 2024J09054), and the Natural Science Foundation of Zhangzhou Municipality (ZZ2023J11).

Notes and references

1 J. Wang, L. Yuan, P. Zhang, J. Mao, J. Fan and X. L. Zhang, *Nanoscale*, 2024, **16**, 7323-7340.
2 L. Collado, A. H. Pizarro, M. Barawi, M. García-Tecedor, M. Liras and V. A. de la Peña O'Shea, *Chem. Soc. Rev.*, 2024, **53**, 11334-11389.
3 L. Wang, S. Wang, M. Li, X. Yang, F. Li, L. Xu and Y. Zou, *J. Alloys Compd.*, 2022, **909**, 164751.
4 Y. Xiong, B. Li, Y. Gu, T. Yan, Z. Ni, S. Li, J. Zuo, J. Ma and Z. Jin, *Nat. Chem.*, 2023, **15**, 286-293.
5 J. Wang, C. Zhao, S. Yuan, X. Li, J. Zhang, X. Hu, H. Lin, Y. Wu and Y. He, *J. Colloid Interface Sci.*, 2023, **638**, 427-438.
6 T. Hu, X. Cheng, J. Luo, Y. Yan, Q. Zhang and Y. Li, *ACS Catal.*, 2024, **14**, 14539-14563.
7 J. Lee, L.-L. Tan and S.-P. Chai, *Nanoscale*, 2021, **13**, 7011-7033.
8 P. Qiu, C. Huang, G. Dong, F. Chen, F. Zhao, Y. Yu, X. Liu, Z. Li and Y. Wang, *J. Mater. Chem. A,* 2021, **9**, 14459-14465.
9 X. Wen and J. Guan, *Nanoscale*, 2020, **12**, 8065-8094.
10 S. Ghoshal, A. Ghosh, P. Roy, B. Ball, A. Pramanik and P. Sarkar, *ACS Catal.*, 2024, **12**, 15541-15575.
11 B. Guo, X. Cheng, Y. Tang, W. Guo, S. Deng, L. Wu and X. Fu, *Angew. Chem. Int. Ed.,* 2022, **61**, e202117244.
12 B. Wang, Y. Zhang and S. D. Minteer, *Energy Environ. Sci.*, 2023, **16**, 404-420.
13 S. Meng, C. Chen, X. Gu, H. Wu, Q. Meng, J. Zhang, S. Chen, X. Fu, D. Liu and W. Lei, *Appl. Catal., B*, 2021, **285**, 119789.
14 S. Ghosh, D. Sarkar, S. Bastia and Y. S. Chaudhary, *Nanoscale*, 2023, **15**, 10939-10974.
15 Y. Zheng, W. Guo, J. Xu and Y. Zhang, *Rev. Inorg. Chem.*, 2025, **45**, 437-452.
16 X. Bian, Y. Zhao, S. Zhang, D. Li, R. Shi, C. Zhou, L.-Z. Wu and T. Zhang, *ACS Materials Lett.*, 2021, **3**, 1521-1527.
17 A. Mallick, C. C. Mayorga-Martinez and M. Pumera, *Chem. Soc. Rev.*, 2025, **54**, 5021-5080.
18 J. Zhao, G. Ren and X. Meng, *Nano Energy*, 2024, **130**, 110109.
19 S. Y. Tee, J. Kong, J. J. Koh, C. P. Teng, X. Wang, X. Wang, S. L. Teo, W. Thitsartarn, M.-Y. Han and Z. W. Seh, *Nanoscale*, 2024, **16**, 18165-18212.
20 H. Yuan, J. Xiao, A.-A. Zhang, Z.-B. Fang and T.-F. Liu, *EnergyChem*, 2025, **7**, 100151.
21 Q. Hu, Y. Liu, W. Li, Y. Wang, W. Liao, H. Zou, J. Li and X. Huang, *Chem. Eng. J.* 2023, **451**, 138670.
22 X. Wang, J. Xu, S. Liu, W. Yang, Y. Chen and Y. Zhang, *Solid State Sci.*, 2022, **129**, 106912.
23 W. Guo, J. Cai, Y. Zheng, W. Xiang, J. Xu and Y. Zhang, *J. Alloys Compd.*, 2025, **1036**, 181882.
24 M. Balci Leinen, D. Dede, M. U. Khan, M. Çağlayan, Y. Koçak, H. V. Demir and E. Ozensoy, *ACS Appl. Mater. Interfaces*, 2019, **11**, 865-879.
25 J. X. Mao, J. C. Wang, H. Gao, W. Shi, H. P. Jiang, Y. Hou, R. Li, W. Zhang and L. Liu, *Int. J. Hydrogen Energy*, 2022, **47**, 8214-8223.
26 X. Wang, S. Liu, R. Ma, W. Yang, Y. Chen, J. Xu and Y. Zhang, *New J. Chem.*, 2023, **47**, 3606-3615.
27 G. K. Thirunavukkarasu, J. Bacova, O. Monfort, E. Dworniczek, E. Paluch, M. B. Hanif, S. Rauf, M. Motlochova, J. Capek, K. Hensel, et al., *Appl. Surf. Sci.*, 2022, **579**, 152145.
28 H. Cui, J. Cao, Y. Zhao, J. Wang, S. Li, K. Ge, J. Chen and Y. Yang, *Chem. Eng. J.*, 2024, **479**, 147618.
29 L.Wang, Z. Zhang, Q. Han, Y. Liu, J. Zhong, J. Chen, J. Huang, H. She and Q. Wang, *Appl. Surf. Sci.*, 2022, **584**, 152645.
30 A. Ziashahabi, R. Poursalehi, N. Naseri and R. Peymani, *J. Mater. Sci. Technol.*, 2022, **17**, 2400-2409.
31 A. Bayles, S. Tian, J. Zhou, L. Yuan, Y. Yuan, C. R. Jacobson, C. Farr, M. Zhang, D. F. Swearer, D. Solti, et al., *ACS Nano*, 2022, **16**, 5839-5850.
32 Y. Zhang, H. Guo, W. Weng and M.-L. Fu, *Phys. Chem. Chem. Phys.*, 2017, **19**, 31389-31398.
33 H. Zhou and Y. Zhang, *Phys. Chem. Chem. Phys.*, 2019, **21**, 21798-21805.
34 J. Cai, X. Li, B. Su, B. Guo, X. Lin, W. Xing, X. F. Lu and S. Wang, *J. Mater. Sci. Technol.*, 2025, **234**, 82-89.
35 F. Liu, J. Deng, B. Su, K.-S. Peng, K. Liu, X. Lin, S.-F. Hung, X. Chen, X. F. Lu, Y. Fang, G. Zhang and S. Wang, *ACS Catal.*, 2025, **15**, 1018-1026.
36 Z. Zhou, W. Guo, T. Yang, D. Zheng, Y. Fang, X. Lin, Y. Huo, G. Zhang and S. Wang, *Chin. J. Struct. Chem.*, 2024, **43**, 100245.
37 B. Su, M. Zheng, W. Lin, X. F. Lu, D. Luan, S. Wang and X. W. Luo, *Adv. Energy Mater.*, 2023, **13**, 2203290.
38 Y. Zhang, F. Gao and M.-L. Fu, *Chem. Phys. Lett.*, 2018, **691**, 61-67.
39 X. Yu, H. Qiu, Z. Wang, B. Wang, Q. Meng, S. Sun, Y. Tang and K. Zhao, *Appl. Surf. Sci.*, 2021, **556**, 149785.
40 S. Wu, J. Zhang, W. Chen, P. Xing, X. Liu, B. Teng, L. Zhao and S. Bai, *J. Mater. Chem. A*, 2021, **9**, 26036-26044.
41 M.-H. Vu, C.-C. Nguyen and T.-O. Do, *ACS Sustainable Chem. Eng.*, 2020, **8**, 12321-12330.
42 J. H. Shah, A. S. Malik, A. M. Idris, S. Rasheed, H. Han and C. Li, *Chin. J. Catal.*, 2021,**42**, 945-952.
43 T. Liu, B. Wang, T. Wang, C. Li, W. Wang, M. Wang and J. Zhang, *Chemosphere*, 2022, **300**, 134621.
44 M. A. Qamar, M. Javed and S. Shahid, *Opt. Mater.*, 2022, **126**, 112211.
45 H. Lee, H. S. Jang, N. Y. Kim and J. B. Joo, *J. Ind. Eng. Chem.*, 2021, **99**, 352-363.
46 Z. Zhang, F. Li, G. Li, R. Li, Y. Wang, Y. Wang, X. Zhang, L. Zhang, F. Li, J. Liu, et al., *J. Solid State Chem.*, 2022, **310**, 123041.
47 J. Ortiz-Bustos, S. Gómez-Ruiz, J. Mazarío, M. E. Domine, I. del Hierro and Y. Pérez, *Catal. Sci. Technol.*, 2020, **10**, 6511-6524.
48 Y. Lan, X. Wang, Y. Chen, J. Xu and Y. Zhang, *Solid State Sci.*, 2023, **146**, 107346.
49 J. Cai, S. Liu, X. Wang, X. Huang, J. Xu and Y. Zhang, *New J. Chem.*, 2024, **45**, 14933-14942.
50 C. L. Chen, H. Y. Wang, J. P. Li, L. S. Long, X. J. Kong and L. S. Zheng, *Inorg. Chem. Front.* 2022, **9**, 2862-2868.

View Article Online
DOI: 10.1039/D5NR02407B

Data Availability Statement

The data supporting this article have been included as part of the Supplementary Information.